

Quantification of MagLIF morphology using the Mallat Scattering Transformation

Michael E. Glinsky,¹ Thomas W. Moore,¹ William E. Lewis,¹ Matthew R. Weis,¹ Christopher A. Jennings,¹ David J. Ampleford,¹ Patrick F. Knapp,¹ Eric C. Harding,¹ Matthew R. Gomez,¹ and Adam J. Harvey-Thompson¹
Sandia National Laboratories, Albuquerque, New Mexico 87185 USA

The morphology of the stagnated plasma resulting from Magnetized Liner Inertial Fusion (MagLIF) is measured by imaging the self-emission x-rays coming from the multi-keV plasma. Equivalent diagnostic response can be generated by integrated radiation-magnetohydrodynamic (rad-MHD) simulations from programs such as HYDRA and GORGON. There have been only limited quantitative ways to compare the image morphology, that is the texture, of simulations and experiments. We have developed a metric of image morphology based on the Mallat Scattering Transformation (MST), a transformation that has proved to be effective at distinguishing textures, sounds, and written characters. This metric is designed, demonstrated, and refined by classifying ensembles (*i.e.*, classes) of synthetic stagnation images, and by regressing an ensemble of synthetic stagnation images to the morphology (*i.e.*, model) parameters used to generate the synthetic images. We use this metric to quantitatively compare simulations to experimental images, experimental images to each other, and to estimate the morphological parameters of the experimental images with uncertainty. This coordinate space has proved very adept at doing a sophisticated relative background subtraction in the MST space. This was needed to compare the experimental self emission images to the rad-MHD simulation images.

I. INTRODUCTION

Magnetized Liner Inertial Fusion (MagLIF) is a magneto-inertial fusion concept currently being explored at Sandia's Z Pulsed Power Facility.^{1–4} MagLIF produces thermonuclear fusion conditions by driving mega-amps of current through a low-Z conducting liner. The subsequent implosion of the liner containing a preheated and premagnetized fuel of deuterium or deuterium-tritium compresses and heats the system, creating a plasma with fusion relevant conditions.

Developing a detailed understanding of how experimental parameters such as premagnetization, preheat, and liner design mitigate losses and affect performance, as well as evolution of the plasma, is a crucial and ongoing step towards realizing the full potential of MagLIF. To this end, time resolved radiography of the imploding liner, as well as self emission x-rays from the plasma at stagnation (where thermal pressure of the plasma stalls the liner implosion), have been used to study the evolution of the plasma and its structure at peak fusion conditions. For example, Awe *et al.*² observed an unexpected feature in radiographs of a magnetized imploding liner – a multi-helix structure not observed in non-magnetized liners. Additionally, axially bifurcated double helical strands have been observed in the stagnating plasma columns, captured by self emission x-ray image diagnostics. See Fig. 1 for an example image of the x-ray self emission from the stagnated plasma. Details of the helical structure vary, such as if there are one or two strands, and may not be resolved in some images since the resolution of the x-ray imager has just recently been improved.

The underlying physics linking the multi-helix structure of the imploding liner to the bifurcated double-helices in the stagnated plasma is as of yet unknown. One working hypothesis is that a helical magnetic Rayleigh-

Taylor instability⁵ (MRT) seeded on the outside liner surface may grow large enough to feed-through the liner to seed perturbations on the liner interior. It is thought that these interior perturbations may imprint the double helical structure on the plasma. It has been experimentally demonstrated that the helical structure is dependent on the aspect ratio of the liner ($AR \equiv$ initial liner outer radius/initial liner wall thickness). Recent experiments with varying liner thicknesses appear to demonstrate, that in the case of uncoated liners, the stagnation column helical radius increases while helical wavelength decreases with increasing AR , which is consistent with MRT feed-through from the outer liner surface.⁶ There is another, less developed, working hypothesis that this double helical structure might be an emergent structure of the nonlinear evolution of the MRT that is controlled by conserved magnetic and cross helicities that are injected into the liner. The large scale self organization would be the result of a Taylor relaxation,⁷ that is an energy minimization under the constraints of the topologically conserved helicities. This is supported by the inverse turbulent cascade in the liner structure seen by Yager-Elorriaga *et al.*⁸ on ultra-thin foils driven at less than 1 MA. However, such inferences remain weak due to the fact that, to date, there has been no systematic way to quantitatively compare stagnation morphology experiment-to-experiment or experiment-to-simulation while accounting for the uncertainty in characterizing features such as the helical wavelength and radius.

In this work, we develop a method which enables such a comparison by applying a cutting edge Machine Learning (ML) algorithm in image classification known as the Mallat Scattering Transform (MST).^{9,10} Specifically, we are able to use the MST as a quantitative metric of morphology to compare stagnation images, and as a metric to infer morphological features with uncertainty via a regression. In Sec. II, we supply the required theory for

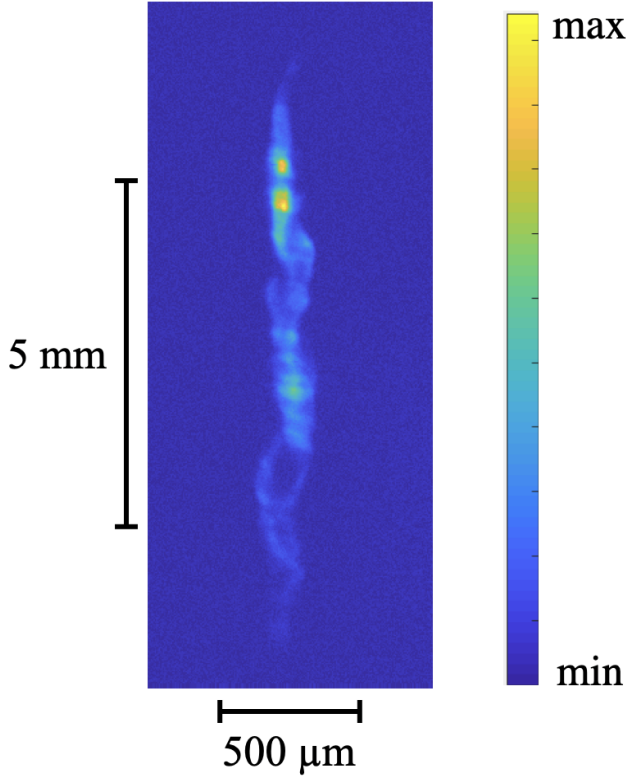


FIG. 1. Self emission x-ray image of plasma stagnation showing double-helix structure (experiment z3236). Axial direction is vertical. Radial direction is horizontal and exaggerated.

the MST, show its connection to Deep Learning, and describe its relationship to causal physics. Section III describes the synthetic model used to parametrize the double helix morphology. We then discuss the design of the image morphology metric based on the MST. This metric is then tested in two ways. The first is via a classification of ensembles of synthetic stagnation images, and the second is via performance of a full machine learning pipeline that quantifies the morphological parameters of the stagnation images with uncertainty via regression. Section III concludes with a verification of the metric design. Section IV demonstrates the application of the metric of image morphology in quantitatively comparing simulation and experiment, as well as a direct extraction of the morphological parameters with uncertainty from experimental images. We highlight the viability of the method to differentiate between plasmas produced from different experimental designs, and the use of the MST to do a sophisticated background subtraction to enable comparison of experiments to simulations.

II. MALLAT SCATTERING TRANSFORM

A. Deep learning based definition of MST

Recently, the use of deep learning methods, combined with availability of large labeled data sets, has enabled a revolution in the field of image classification and analysis. Particularly, Convolutional Neural Networks (CNNs) have gained widespread popularity for image analysis problems, such as classification,¹¹ segmentation,¹² and even image generation.¹³ The ubiquity of this approach is largely based on the ability of CNNs to learn convolutional filters which compute features that are approximately invariant to irrelevant symmetries present in the task (*e.g.* translation or rotational symmetries).¹⁴

However CNNs require significant expertise to navigate a seemingly arbitrary design space (*e.g.*, number of nodes and layers) and require considerable computing resources to train, even when using transfer learning. Additionally, their *black box* nature make CNNs a less attractive framework for scientific applications to bridge the gap between causation and correlation. Alternative kernel classifiers such as the probabilistic neural network, are based on the Euclidean distance between image features (*e.g.*, pixel information), which is easily broken by transformations, rotations and scaling. At the same time, familiar translation invariant feature representations such as the Fourier transform modulus are unstable to deformations (that is not Lipschitz continuous). The wavelet transformation on the other hand, is Lipschitz continuous to deformation, but is not translation invariant.¹⁰ By combining local translation invariance and Lipschitz continuity to deformations in a fixed weight convolutional network, the MST addresses many of the concerns that arise in deep learning.^{9,10}

The MST consists of compositions of wavelet transformations coupled with modulus and non-linear smoothing operators which form a deep convolutional network. Unlike deep convolutional neural networks, the filters in the MST are prescribed rather than learned. In fact the deep convolutional network of the MST has been shown to outperform CNNs for image classification tasks over a broad range of training sample sizes.¹⁰ This is most significant when the amount of training samples is considerably limited,¹⁰ which is often the case with experimental data. Additional benefits of the MST framework over CNNs come in the form of intelligible design – for example, the depth of an MST network is bound by a signal’s energy propagation through the network, whereas the depth of a CNN is seemingly arbitrary.

The two-dimensional MST uses a set of convolutional filters which are calculated from a Mother Wavelet ψ by applying a rotation r and scaling by 2^j :

$$\psi_\lambda = 2^{-2j} \psi(2^{-j} r^{-j} u), \quad (1)$$

where $\lambda = 2^{-j} r$ and u is the spatial position. Let the wavelet transformation of image $x(u)$ be given by $x \star \psi_\lambda$.

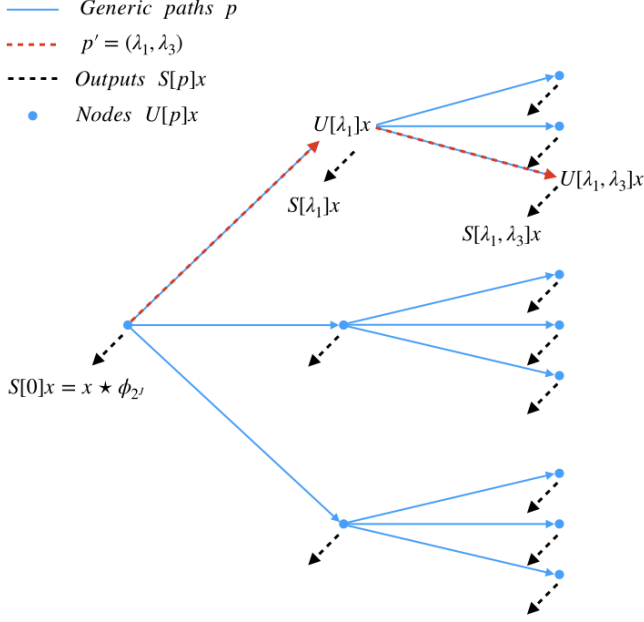


FIG. 2. The MST may be thought of as a convolutional network with fixed weights. The above network could represent for example a 1D MST with 3 scales, and no rotations (1D case). The network outputs MST coefficients averaged by a Father Wavelet along each path, $S[p]x$. Each node of the network is the set of scattering coefficients before being window averaged by the Father Wavelet, $U[p]x$. The operator \tilde{W} of Eq. (4) expands the network below a given node at then at the end of a path, p .

Given that the spatial resolution is retained in a wavelet transform, this process can be iterated upon, such that the propagated signal along path $p = (\lambda_1, \lambda_2, \dots, \lambda_m)$ is given by:

$$U[p]x = U[\lambda_m] \dots U[\lambda_2]U[\lambda_1]x \\ = |||x \star \psi_{\lambda_1}| \star \psi_{\lambda_2}| \dots | \star \psi_{\lambda_m}| \quad (2)$$

where the modulus removes the complex phase from the propagated signal. However, the wavelet coefficients are not invariant to translation, but rather translation covariant. Introducing the Father Wavelet (*i.e.*, a spatial window function), $\phi_{2^J}(u) = 2^{-2J}\phi(2^{-J}u)$, allows an average pooling operation to be performed by convolution $U[p]x \star \phi_{2^J}(u)$. This operation collapses the spatial dependence of the wavelet coefficients while retaining the dominant amplitude $U[p]$ at each scale. This results in an effective translation invariance assuming that a given translation is much smaller than the window scale, 2^J . The windowed scattering transformation is thus given by:

$$S[p]x(u) = U[p]x \star \phi_{2^J}(u) \\ = |||x \star \psi_{\lambda_1}| \star \psi_{\lambda_2}| \dots | \star \psi_{\lambda_m}| \star \phi_{2^J}(u). \quad (3)$$

Now, we may define an operator \tilde{W} which acts upon the non-windowed scattering $U[p]x$ producing

$$\tilde{W}U[p]x = \{S[p]x, U[p+\lambda]x\}_{\lambda \in \mathcal{P}}. \quad (4)$$

\tilde{W} will produce the output scattering coefficient at the current layer for the given path p , and will move to the next layer along the path $p+\lambda$ as demonstrated in Fig. 2. With Eqns. (2) and (3), we arrive at a deep scattering convolutional network \tilde{W} in Eq. (4) with m layers. For 2-D signals (images), the MST coefficients are visualized via log polar plots as depicted in Fig. 3.

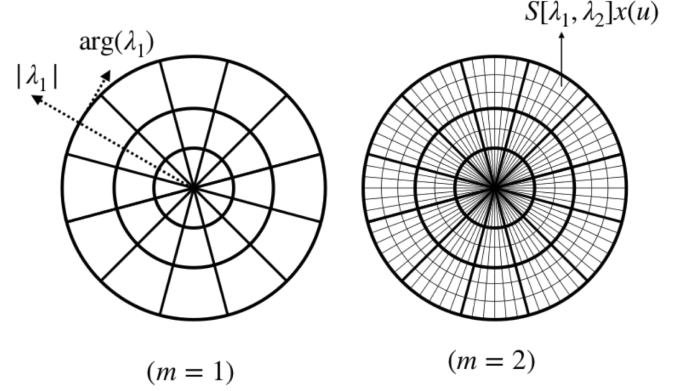


FIG. 3. Coefficients produced by applying MST to 2D images in this work will be displayed on radial plots as shown. Bins are created according to scale (radial positioning, $|\lambda_m|$, and rotation, $\arg(\lambda_m)$) with magnitude (color scale, not shown) representing the size of the coefficient at that scale and rotation.

The MST forms a nonlinear mapping from an image's spatial features to its scale features. This mapping is Lipschitz continuous to deformation, meaning that small deformations of the image result in small deformations of the Mallat scattering coefficients. Since we will be concerned with discovering morphology parameters of stagnation column images such as helical wavelength, the MST provides a convenient basis as compared to, for example, a Fourier transform which is not Lipschitz continuous to deformations. The first order MST, $m = 1$, can be viewed as an optimal “local” Fourier transform. The reader is referred to Mallat⁹ and Bruna and Mallat¹⁰ for more details regarding the mathematical properties of MST, such as being a unitary transformation, and having a scale ordering of the path, p .

B. Physical foundation of MST

In the previous Sec. IIA, we developed the MST as a deep convolutional network with a very specific form. There was no physical reason given (other than desiring the mathematical properties of Lipschitz continuity and stationarity) for the design choices such as: the use of iterative convolution with a Mother Wavelet, the use of the modulus as an activation function between layers, and the final pooling using convolution with the Father Wavelet. There was also no reason given for: the sparseness of the MST, the need for only the first and second or-

der MST, and the efficacy of the MST as a representation for the Machine Learning of physical systems. As it turns out, there could be deep physical foundations for these design choices that explain its compactness and efficacy. These connections were briefly mentioned in Mallat⁹ and are alluded to by the use of the word “Scattering” in the name of the transformation.

Important properties that connect the MST to causal dynamics have been noted in the previous section. Fundamental to these connections is the fact that physical dynamics, whether it be fluid dynamics, classical mechanics, or quantum field theory is built upon advection (*i.e.*, deformation) by a vector field, which is also how physical symmetries are generated. This is why having Lipschitz continuity is paramount. Imposing this constraint on the transformation limits the representation to physically realizable systems with the proper symmetries. Furthermore, the construction of the MST also leads to the properties that the transformation is unitary (expressing that probability can not be created or destroyed), and that the path is scale ordered (expressing that the system is causal). Furthermore, the convolution by the Father Wavelet and the use of the modulus might be viewed as an expectation value operator and the evaluation of Gaussian integrals via the method of stationary phase, respectively.

Another seemingly arbitrary choice is the truncation of the MST expansion at second order. It could be that a physical system that encodes finite information is fully identified by the first and second order MST. This could be because of a statistical realizability theorem¹⁵ – either the distribution stops at second order or it must continue to all orders. Since the dynamical information is finite, the distribution must stop at second order. Practically, it is found that there is little signal energy in the MST of third order and higher, and that there is almost no improvement in the classification or regression performance by including the third order MST.

Finally, it is worth noting that, in the context of images, the MST could be encoding the static scale structure in the first order transform, and the relationship between structures of different scales in the second order transform. This scale-to-scale correlation might be essentially a two-point correlation function between different locations in the image, and the first order transform could be the single-point correlation function. In the context of dynamical systems, this could be analogous to the single-particle and two-particle distribution functions in the Mayer Cluster expansion of classical kinetic theory and the equivalent constructs of quantum field theory. These quantities would encode all the dynamics of the system, meaning that the MST could have a profound connection to the underlying physical dynamics of the system. Significant theoretical and numerical work is well underway to support these physical foundations of the transformation.^{16,17}

III. SYNTHETIC MODEL, CLASSIFICATION AND REGRESSION

A. Synthetic double helix model

In order to quantify the morphology of the MagLIF stagnation column, a model with well defined parameters is needed to act as a surrogate for the x-ray self emission diagnostic images. This model must capture the essential features of the stagnation such as its multi-helical nature, finite axial extent and axial bifurcations. For this purpose, we have constructed a synthetic model complete with 11 descriptive model parameters that capture some features of a fundamentally 3D stagnating plasma projected into a 2D image along with 6 stochastic parameters to represent the *natural* experimental variation and signal noise inherent in the x-ray diagnostics fielded on Z.

Analytically, the synthetic model consists of superimposed “radial” and axial Gaussians over a pair of axial \cos^2 waves. Here, the radial position projected onto the image will be given by r , and the axial position of the image will be given by z . The model may be specified by the composition of the following functions:

$$s(z) = \theta_6 \cos^2(\theta_7 * \theta_3 * z + \zeta_5) + \theta_9 \cos^2(\theta_{10} * \theta_3 * z + \zeta_6), \quad (5)$$

$$r_{0,j}(z) = (-1)^{1+\delta_{j,2}} \theta_8 + \theta_5 \sin(\theta_3 * z + \zeta_4 + \delta_{j,2} \theta_{11}), \quad (6)$$

$$g_j(r, r_{0,j}(z)) = \frac{1}{\theta_1 \sqrt{2\pi}} \exp \left\{ -\frac{(r - r_{0,j}(z))^2}{2\theta_1^2} \right\}, \quad (7)$$

$$\ell(z) = \frac{\zeta_3}{\theta_2 \sqrt{2\pi}} \exp \left\{ -\left(\frac{z^2}{2\theta_2^2} \right)^{\theta_4} \right\}, \quad (8)$$

and

$$h(r, z) = A \sum_{j=1}^2 \left[(1 + s(z)) g_j(r, r_{0,j}(z)) \ell(z) \times (1 - \zeta_2 U(0, 1)) + \zeta_1 U(0, 1) \right], \quad (9)$$

where $h(r, z)$ is the final composition used to generate double helix images, $\ell(z)$ is the axial envelope, g_j is the Gaussian envelope of the helical strand, $r_{0,j}(z)$ is the center of the helical strand, $s(z)$ is axial bifurcations of the helical strands, $U(0, 1)$ is a uniformly distributed random number on $[0, 1]$, $j \in \{1, 2\}$ is the strand index, $\delta_{i,j}$ is the Kronecker delta function, A is a constant used to normalize the max value of $h(r, z)$ to unity, and (θ_i, ζ_i) will be described.

The θ_i and ζ_i parameters are depicted in Fig. 4 and summarized in Table I. Their interpretations are: θ_1 is the standard deviation of the radial Gaussian, θ_2 is the

standard deviation of the axial Gaussian, θ_3 is the Magneto Rayleigh-Taylor (MRT) wavenumber, θ_4 is the order of the super Gaussian, θ_5 is the helical strand radius, θ_6 is the amplitude of the large-wavelength axial bright spot, θ_7 is the mode of the large-wavelength axial bright spot, θ_8 is the strand separation, θ_9 is the amplitude of the small-wavelength axial bright spot, θ_{10} is the mode of the small-wavelength axial bright spot, and θ_{11} is the strand phase; ζ_1 is the background noise, ζ_2 is the signal noise, ζ_3 is the amplitude of the signal, ζ_4 is the radial perturbation phase shift, ζ_5 is the phase shift of the large-wavelength axial bright spot, and ζ_6 is the phase shift of the small-wavelength axial bright spot.

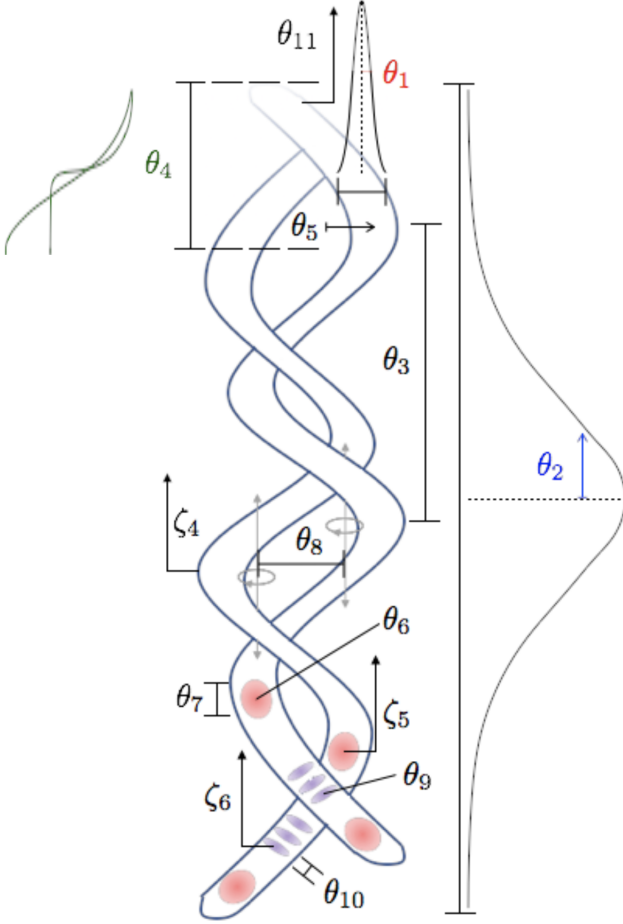


FIG. 4. Synthetic Stagnation Model (see Table I).

B. Metric design

A majority of the design decisions including gridding, maximum MST order, variable transformations, normalization, and scale resolution are inherited from Bruna and Mallat¹⁰'s use of deep scattering transformation networks for handwritten digit recognition from the MNIST database of handwritten digits. With this being said,

TABLE I. Synthetic model θ_i and stochastic ζ_i parameters (see Fig. 4).

Model Parameters

θ_1 = thickness
θ_2 = length
θ_3 = helical wavenumber
θ_4 = order of axial super Gaussian
θ_5 = amplitude of radial perturbations
θ_6 = amplitude of large-wavelength axial brightness perturbations
θ_7 = mode number of large-wavelength axial brightness perturbations
θ_8 = strand separation
θ_9 = amplitude of small-wavelength axial brightness perturbations
θ_{10} = mode number of small-wavelength axial brightness perturbations
θ_{11} = relative strand phase
θ_{12} = strand ratio

Stochastic Parameters

ζ_1 = background noise
ζ_2 = signal noise
ζ_3 = amplitude of signal
ζ_4 = radial perturbation phase shift
ζ_5 = large-wavelength axial brightness perturbations phase shift
ζ_6 = small-wavelength axial brightness perturbations phase shift

these design decisions were verified by examining the effect on the regression performance of alternative design decisions. See Sec. III E, for the verification.

We now discuss how metric features were engineered. First, the reader may note from Eq. (3) that we must evaluate the scattering coefficients at points u in our image. Now, due to the assumption that the statistics given by the MST are stationary, that is spatially invariant, below the Father Wavelet window size; if we were to evaluate $S[p]x(u)$ at all points u , one would obtain very redundant information. As a result, it is wise to subsample u . This is achieved by translating the spatial window by intervals of 2^J such that $G_{\#} = N2^{-J}$, where N is the symmetric pixel count and $G_{\#}$ is symmetric grid number. This subsampling forces each image to be segmented into a $G_{\#} \times G_{\#}$ -grid.¹⁰ We work with images of pixel size 512×512 , and set $J = 7$ giving $G_{\#} = 4$. We now have a design parameter to choose, J , which determines the size of the sub-image, $2^J \times 2^J$, over which the transform will be calculated. This was chosen based on the position, size and characteristics of our double helix (see Fig. 5) and was found to give good regression performance as discussed later. We note however, that a more rigorous procedure to select J would be to select the J which gives maximum cross validated classifier or regression performance. With this being said, our eyes are very good at recognizing the dynamical space scale of the physics. The size of the Father Wavelet, 2^J , should be of this scale. If the size is too small, the MST will not be calculated

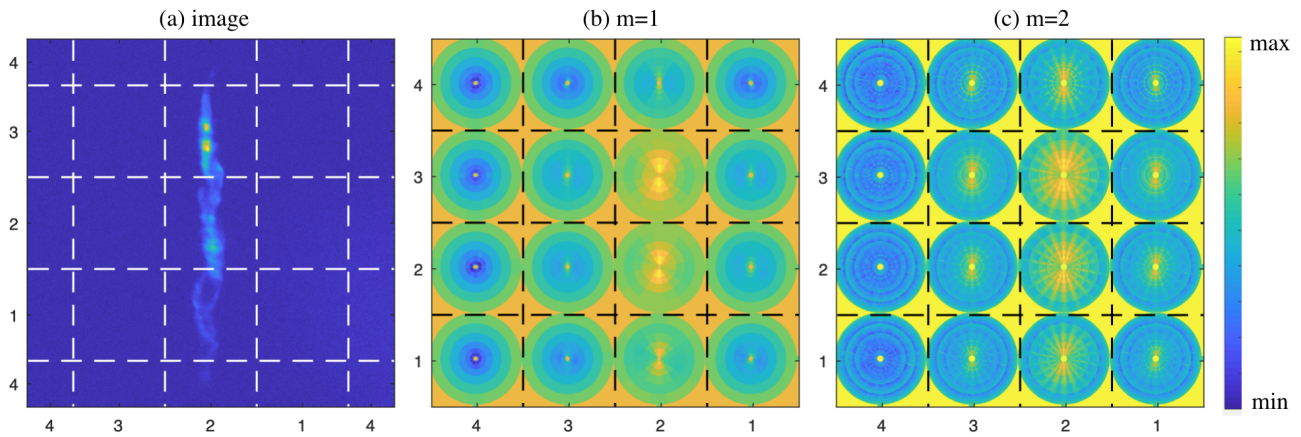


FIG. 5. Gridded MST: (a, left) self emission image of experiment z3236, (b, center) first and (c, right) second order MST coefficients.

over the largest area possible and will therefore have more noise and not contain as much statistical information. If the size is too large, the assumption of stationarity will be violated leading to a blurring of the statistics and a resulting loss of information. It is therefore expected that there will be an optimal size that could be determined by the aforementioned J cross validation optimization.

An added benefit to gridding the images, is data reduction via patch selection. From Fig. 5(a) it is apparent that most of the image is background noise. This is echoed in the MST coefficient space. Since our double helix is confined to column 2, essentially all of the unique information is contained within the MST coefficients evaluated on the four patches in column 2, so that the other columns may be dropped. We also only calculate the MST to second order, $m = 2$. Before computing the MST on our gridded image, we must apply boundary conditions for the convolution. There are many reasonable choices, such as periodic, zero-padded, and mirrored. We chose to use a mirror boundary condition. This minimized the influence of the boundary, while making the minimum assumption about the signal outside of the domain.

The final step in engineering features for a machine learning algorithm is to perform an appropriate scaling of the input features. This is a common practice in statistical learning, and many different scaling transformations and dimensionality reduction methods are reasonable. Here, we apply a \log_{10} scaling to our scattering coefficients and model parameters (with the exception of θ_{11} which is a phase shift) used in training the classifier. This choice was made to decrease the dynamic range of the MST coefficients, since before the transformation the MST coefficients were dominated by only a few coefficients.

C. Classification model

Studying the ability of the MST to distinguish between different classes of helical morphology will quantify the performance of the MST as a metric of image morphology and will provide reassurance that the regression problem is well-posed. Additionally, it provides access to more easily interpretable results (*e.g.*, classification accuracy as opposed to R^2). By considering the classification problem, we are also able to closely follow the approach using the MST for MNIST handwritten digit recognition in Bruna and Mallat¹⁰.

We approach the problem by synthesizing 12 stagnation image classes – 11 distinct parameter constrained classes constructed from systematic modifications to the synthetic model parameter distributions from a single base class. Each of the distinct parameter classes has a definitive associated synthetic model parameter. For a given parameter class, the distribution of its associated synthetic model parameter is translated some separation from its corresponding base class distribution. This process is repeated for each of the 11 distinct parameter classes (see Fig. 6). For the classification problem, we generate 340 images. We use 50% of this data set as the training set to train an affine classifier, while the remaining 50% is separated out as the test set to be used for characterizing the trained classifier.

Finally, we apply the classification algorithm. Following Bruna and Mallat¹⁰, we apply a classifier based on an affine space model with the approximate affine space determined by Principal Component Analysis (PCA) of each class. To be specific, let SX_k denote the set of MST coefficients for all of our images belonging to class k . SX_k can be organized into a $N_{i,k} \times P$ matrix where $N_{i,k}$ is the number of images available for class k and P is the number of scattering coefficients (*i.e.*, the coefficients have been stacked into a vector of length P). The columns of Δ_k may be transformed to have zero mean for each of the P coefficients $\Delta_k = SX_k - \mathbb{E}(SX_k)$. We

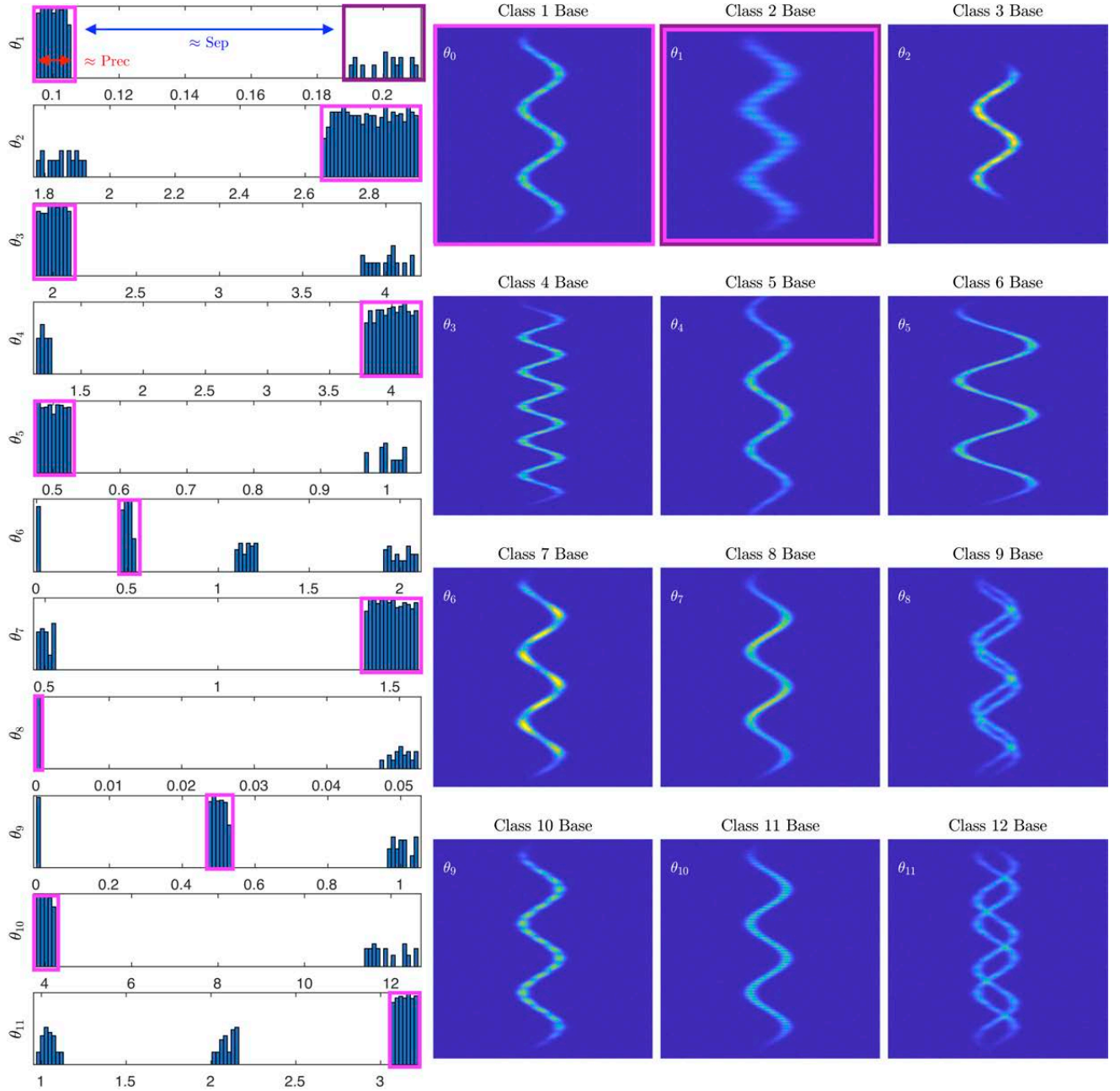


FIG. 6. Classification Training Set construction. Parameter distributions are shown at left while the base classes are represented on the right. Shown is the class separation between class 1 and 2 as the blue line labeled “Sep”, and the class precision of class 1 as the red line labeled “Prec”. Ensemble of synthetic stagnation images for classification (Multimedia View). Shown are the base case (left), the base case for the class (middle), and the individual members of the ensemble (right).

may then perform principal component analysis on Δ_k by finding the eigenvectors $\{\mathbf{U}_{j,k}\}_{j=1}^P$ and corresponding eigenvalues $\{\Lambda_j\}_{j=1}^P$ of the covariance matrix $\Delta_k^T \Delta_k$. Taking $\mathbf{U}_{j,k}$ to be ordered such that $\Lambda_j > \Lambda_{j+1}$, we keep only the first $d \ll P$ principal vectors $\{\mathbf{U}_{j,k}\}_{j=1}^d$. Letting $\mathbf{V}_k = \text{span}(\{\mathbf{U}_{j,k}\}_{j=1}^d)$, we may construct the affine approximation space for class k

$$\mathbf{A}_k = \mathbb{E}(S X_k) + \mathbf{V}_k. \quad (10)$$

Finally, for a new image with scattering coefficients Sx , the class assigned to the image is given by

$$\hat{k}(x) = \underset{k}{\operatorname{argmin}} \|Sx - P_{\mathbf{A}_k}(Sx)\|. \quad (11)$$

In order to evaluate how effectively the classes are separated one may define the ratio of the expected value of the distance of class i to the affine space for class j divided by the expected value of the distance of class i to

its own affine space,

$$R_{ij}^2 \equiv \frac{E(\|SX_i - P_{\mathbf{A}_j}(SX_i)\|^2)}{E(\|SX_i - P_{\mathbf{A}_i}(SX_i)\|^2)}. \quad (12)$$

Note that if the classes are well separated, then R_{ij}^2 will be very large for $i \neq j$, while $R_{ii}^2 = 1$. It thus makes sense to define the matrix

$$\Omega_{ij} = N_j e^{-|R_{ij}|}, \quad (13)$$

where N_j is a column-wise normalization ensuring that each column of Ω_{ij} sums to 1. The off-diagonal elements are indicative of overlap among the tails of the class distributions. This gives a rough probability that members of class j would have values that would be classified as class i , that is the confusion matrix, $P(C_i|C_j)$. For the case that there is small overlap in the class distribution and there are limited samples, Ω_{ij} is a high fidelity surrogate for the confusion matrix. Figure 7 shows the matrix Ω_{ij} for our case demonstrating good class separation as indicated by the fact that the matrix is strongly diagonal. The chance of miss-classification is extremely small ($< 0.1\%$), and the average class precision is 0.00017 while the average class separation is 10. Here we have used the definitions of class separation, R_d^2 , and precision, r_d^2 , given in Bruna and Mallat¹⁰,

$$R_d^2 \equiv \frac{1}{N_c} \sum_{i=1}^{N_c} \frac{E(\min_{j \neq i} \|SX_i - P_{\mathbf{A}_j}(SX_i)\|^2)}{E(\|SX_i - P_{\mathbf{A}_i}(SX_i)\|^2)}, \quad (14)$$

$$r_i^2 \equiv \frac{E(\|SX_i - P_{\mathbf{A}_i}(SX_i)\|^2)}{E(\|SX_i\|^2)} \quad (15)$$

and

$$r_d^2 \equiv \frac{1}{N_c} \sum_{i=1}^{N_c} r_i^2. \quad (16)$$

Note that the separation is just the average of the separation matrix given in Eq. (12). The geometric meaning of the separation and precision are shown in Fig. 6.

Increasing the dimension of the PCA affine approximation space has been shown to make the MST more robust to rotations by effectively reducing the spread of the intra-class affine space while increasing the spread of the inter-class separations for classification problems using an affine classifier and the MST.¹⁰ Here we observe a similar effect of affine space dimensionality on performance as demonstrated in Fig. 8. While the performance is maximized for a dimension of 10, there are diminishing returns after a dimension of 4.

D. Regression model and ML pipeline

We now consider the regression problem as highlighted in Fig. 9. This Machine Learning (ML) pipeline takes as

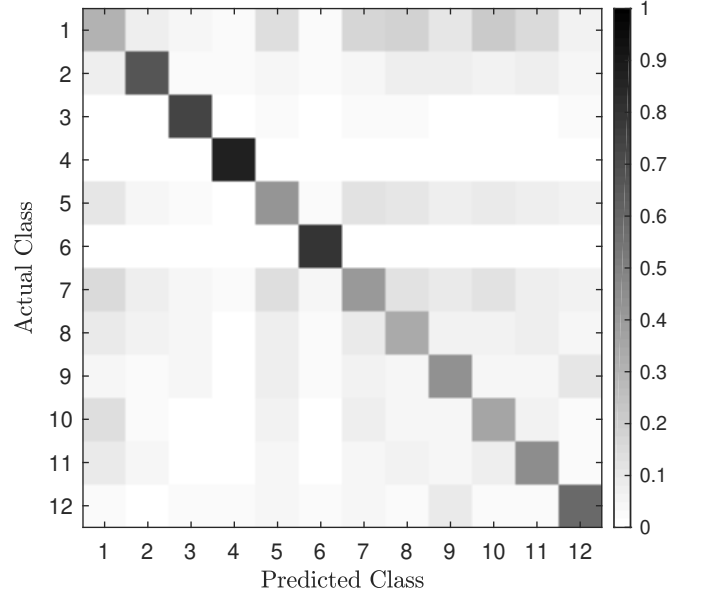


FIG. 7. The surrogate confusion matrix Ω_{ij} defined by Eq. (13) which demonstrates that the constructed double helix classes are well separated in the MST space.

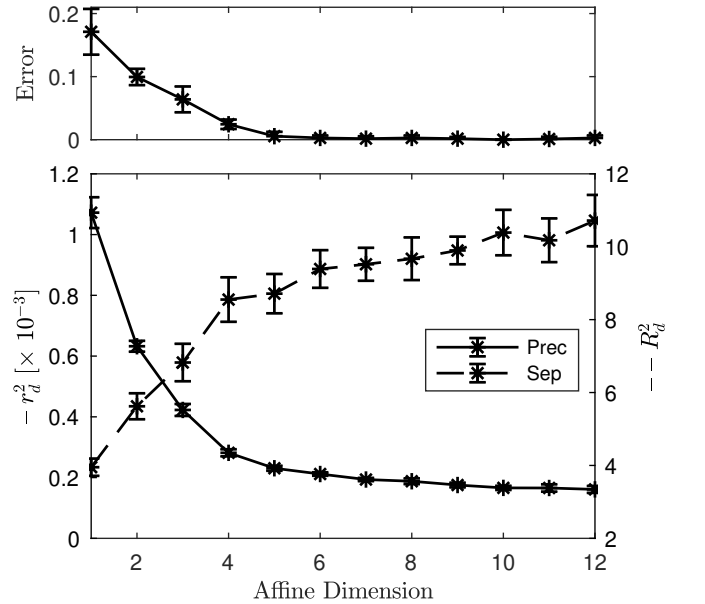


FIG. 8. Optimization curve for the dimension of the affine space. As the dimension of the affine space increases the error decreases and the average intra-class precision (r_d^2) decreases while the inter-class separation (R_d^2) increases.

input an image of a plasma stagnation column and outputs a set $\{\theta_i\}_{i=1}^{11}$ characterizing the morphology of the column along with an estimate of the uncertainty of the output. This will be achieved by creating a set of synthetic images from Eq. (9) using a large set of randomly chosen (θ_i, ζ_i) , computing the MST, and performing a regression from MST coefficients to θ_i . Note the absence of ζ_i in our output as those are meant to represent unim-

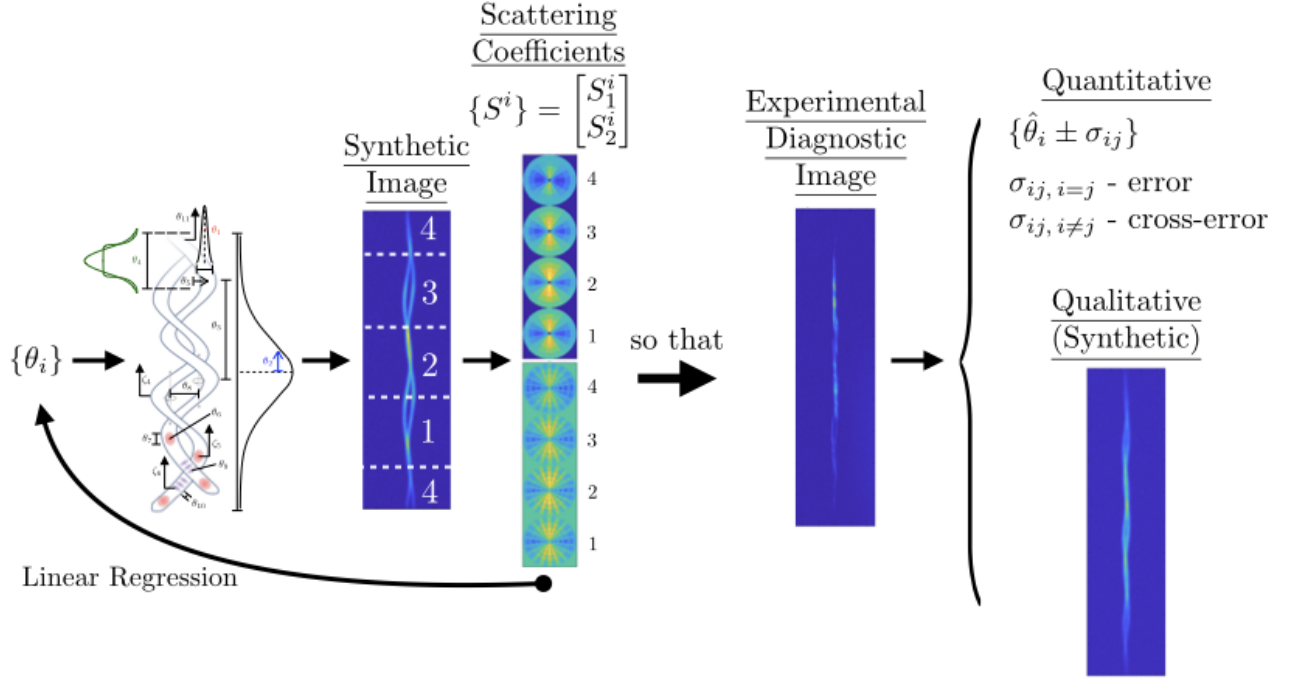


FIG. 9. The MST regression pipeline for morphology characterization of experimental stagnation images. Ensemble of synthetic stagnation images for regression (Multimedia View). Shown are the individual members of the ensemble (left), and the corresponding synthetic stagnation image constructed from the MAP parameters regressed from the MST of the member of the ensemble (right).

portant transformations, such as rotating the viewing angle, which does not alter the fundamental morphology. Specifically, image realizations are produced, using the synthetic model, from a random sampling of the log-uniformly distributed model parameters. The statistical properties of these distributions are determined by visually confirming that helices produced encompass what is reasonable to expect from experiment. Additionally, most of the quantities we wish to learn from the helical images (*i.e.* the θ_i 's) are non-negative. As a result, we chose to \log_{10} scale all of the θ_i values except for the strand phase θ_{11} .

Before conducting a linear regression from (\log_{10} scaled) MST coefficients to (scaled) helical parameters, we standard normal scale θ and \mathbf{S} . We will henceforth refer to the transformed quantities as $\tilde{\theta}$ and $\tilde{\mathbf{S}}$. Principal Component Analysis (PCA) is then employed to find a set of orthonormal basis vectors by which to rotate the MST coefficients and model parameters into a more directly correlated space, prior to linear regression, by applying Singular Value Decomposition (SVD) to the cross-covariance between the MST coefficients and model parameters from the training set, $\text{CCOV}(\tilde{\theta}, \tilde{\mathbf{S}}) = \tilde{\theta}^T \tilde{\mathbf{S}} / (N - 1)$. Here, N is the number of training samples used to construct the cross-covariance. The SVD factors the cross-covariance matrix into a set of transformation matrices \mathbf{U} and \mathbf{V} bounding a diagonal matrix Σ con-

taining a set of singular values

$$\mathbf{U} \Sigma \mathbf{V}^T = \frac{\tilde{\theta}^T \tilde{\mathbf{S}}}{N - 1}. \quad (17)$$

PCA is often used on linear systems for dimensionality reduction, however for reasons that will be discussed shortly, we retain full dimensionality. This set of transformation matrices provides a set of orthogonal basis vectors along which $\tilde{\theta}$ and $\tilde{\mathbf{S}}$ are most directly correlated, ordered from strongest to weakest correlation (see Fig. 10 and Fig. 11). Most of the correlation is contained in the first four dimensions, about 91% of the variation. The model parameters $\tilde{\theta}$ and scattering coefficients $\tilde{\mathbf{S}}$ are rotated into the directly correlated space such that $\mathbf{Y} = \tilde{\theta} \mathbf{U}$ and $\mathbf{X} = \tilde{\mathbf{S}} \mathbf{V}$ define the rotated variables.

Regressing the rotated scattering coefficients \mathbf{X} back onto the rotated \mathbf{Y} is accomplished using multidimensional linear regression,

$$Y_j = b_j + \sum_{i=1}^p X_i m_{ij} + \epsilon_j, \quad (18)$$

where \mathbf{m} is the map from \mathbf{X} to \mathbf{Y} (*e.g.*, “slope”), \mathbf{b} is the bias (*e.g.*, intercept), ϵ is the error term, and $\epsilon = \mathcal{N}(0, \mathbf{\Lambda})$ is assumed to be a zero mean normal random variable with covariance matrix $\mathbf{\Lambda}$. Writing Eq. (18) in matrix notation, the bias is absorbed into the slope such that $\mathbf{Y} = \mathbf{X} \mathbf{M} + \epsilon$.

Note that Eq. (18) implies that the prediction for a new input \mathbf{X} is $\mathbf{Y}_{\text{pred}} = \hat{\mathbf{Y}} = \mathbf{X}\mathbf{M}$ since $\bar{\epsilon} = 0$. Importantly, this would also be able to characterize the uncertainty in our prediction if we had an estimate of $\mathbf{\Lambda}$. In order to estimate \mathbf{M} and $\mathbf{\Lambda}$, note that Eq. (18) specifies a likelihood function

$$P(\{\mathbf{Y}_i\}|\mathbf{M}, \mathbf{\Lambda}, \{\mathbf{X}_i\}) = \prod_{i=1}^N \frac{1}{\sqrt{(2\pi)^k |\mathbf{\Lambda}|}} \times e^{-\frac{(\mathbf{Y}_i - \mathbf{X}_i \mathbf{M})^T \mathbf{\Lambda}^{-1} (\mathbf{Y}_i - \mathbf{X}_i \mathbf{M})}{2}}, \quad (19)$$

where the training data are assumed i.i.d. and k is the dimensionality of our output space (here $k = 11$ since there are 11 theta parameters to which we wish to regress). A maximum likelihood estimate of the coefficients of the map matrix \mathbf{M} and error covariance matrix $\mathbf{\Lambda}$ are determined by finding their values which maximize the likelihood function over our training data. Equivalently, since the logarithm is monotonic, we may maximize the log-likelihood \mathcal{L} . The solution is derived in many statistics and machine learning textbooks (see *e.g.* Bishop¹⁸) and is given by

$$\mathbf{M}_{\text{MLE}} = (\mathbf{X}^T \mathbf{X})^{-1} \mathbf{X}^T \mathbf{Y}, \quad (20)$$

which is the typical ordinary least squares solution where $\mathbf{X}_i(\mathbf{Y}_i)$ have been stacked to create $\mathbf{X}(\mathbf{Y})$ and the error covariance matrix is

$$\mathbf{\Lambda}_{\text{MLE}} = \frac{1}{N} \sum_{i=1}^N (\mathbf{Y}_i - \mathbf{X}_i \mathbf{M}_{\text{MLE}})^T (\mathbf{Y}_i - \mathbf{X}_i \mathbf{M}_{\text{MLE}}), \quad (21)$$

which is just the estimate of the population covariance matrix of the difference $(\mathbf{Y} - \mathbf{Y}_{\text{pred}})$.

For a new image, we can now estimate a set of values θ along with an estimate of the uncertainty on theta according to the following algorithm:

1. Compute the first and second order scattering coefficients of the image on a 4x4 grid (see Figure 5).
2. Discard all but the second column from the grid for each of the 2 sets of coefficients.
3. Compute \log_{10} of the scattering coefficients and flatten into a vector to get \mathbf{S} .
4. Standard normal scale using the mean and standard deviation estimated on the training set to get $\tilde{\mathbf{S}}$.
5. Project onto principal components to get $\mathbf{X} = \tilde{\mathbf{S}}\mathbf{V}$.
6. Compute $\mathbf{Y}_{\text{pred}} = \mathbf{X}\mathbf{M}_{\text{MLE}}$.
7. Create a set of values consistent to within the error term

$$\{\mathbf{Y}_{\text{pred},i}\}_{i=1}^{N_{\text{resamp}}} = \mathbf{Y}_{\text{pred}} + \{\mathcal{N}_i(0, \mathbf{\Lambda}_{\text{MLE}})\}_{i=1}^{N_{\text{resamp}}}.$$

8. Compute $\{\tilde{\theta}_i\} = \{\mathbf{Y}_{\text{pred},i} \mathbf{U}^{-1}\}$.

9. Compute $\{\theta_i\}$ by inverting standard normal scaling of $\tilde{\theta}$ using the mean and standard deviations of $\tilde{\theta}$ computed from the training set and then invert the \log_{10} scaling performed on all but the last component of θ .

10. We now have an estimate of the distribution of θ consistent with the original image. We may report the prediction and error as means and standard deviations, or as percentiles (*e.g.*, report the 50th percentile as the prediction and the 2.5-percentile and 97.5-percentile as lower and upper bounds).

In our case, inverting the transformations leads to an asymmetric distribution of θ values consistent with the original image, so here we will report the 95% confidence interval and the mode of the distribution rather than mean and standard deviation for any predictions.

Before moving on to discuss results, we note that the cross-covariance matrix computes the a set of basis vectors along which the quantities $\tilde{\theta}$ and $\tilde{\mathbf{S}}$ exhibit the strongest linear correlation. As a result, any nonlinear relationships between $\tilde{\theta}$ and $\tilde{\mathbf{S}}$ will not be recoverable upon linear regression. First attempts using a linear regression given by Eq. (20), when truncating the dimensionality of the principle components to the number of singular values, showed nonlinear bows. A more generalized model was constructed to capture this nonlinear behavior by including the full SVD.

A slight modification to the predictive model is required to mitigate numerical issues with this more generalized model. This is a repercussion of using the full SVD on the cross-covariance matrix which causes the quantity $\mathbf{X}^T \mathbf{X}$ from Eq. (20) to be ill-conditioned. Applying $L2$ -regularization to the predictive model is shown to be an effective mitigation procedure. The predictive model with $L2$ -regularization is

$$\hat{\mathbf{Y}} = \mathbf{X}(\mathbf{X}^T \mathbf{X} + \lambda \mathbf{I})^{-1} (\mathbf{X}^T \mathbf{Y}) \quad (22)$$

where λ is optimized through cross-validation, maximizing R^2 , where

$$R^2 \equiv 1 - \frac{\sum_i (\mathbf{Y}_i - \hat{\mathbf{Y}}_i)^2}{\sum_i (\mathbf{Y}_i - \bar{\mathbf{Y}})^2}. \quad (23)$$

We find that the optimum value of λ_{CV} is 0.005614.

Image realizations ($N = 2048$) are produced, using the synthetic model, from a random sampling of the log-uniformly distributed model parameters. The statistical properties of these distributions are determined by visually confirming that helices produced encompass what is reasonable to expect from experiment. For each θ realization, a set of features is extracted from its corresponding synthetically generated image using the MST. The data set is randomly separated into a training (50%), validation (25%), and test (25%) sets. The training set is used

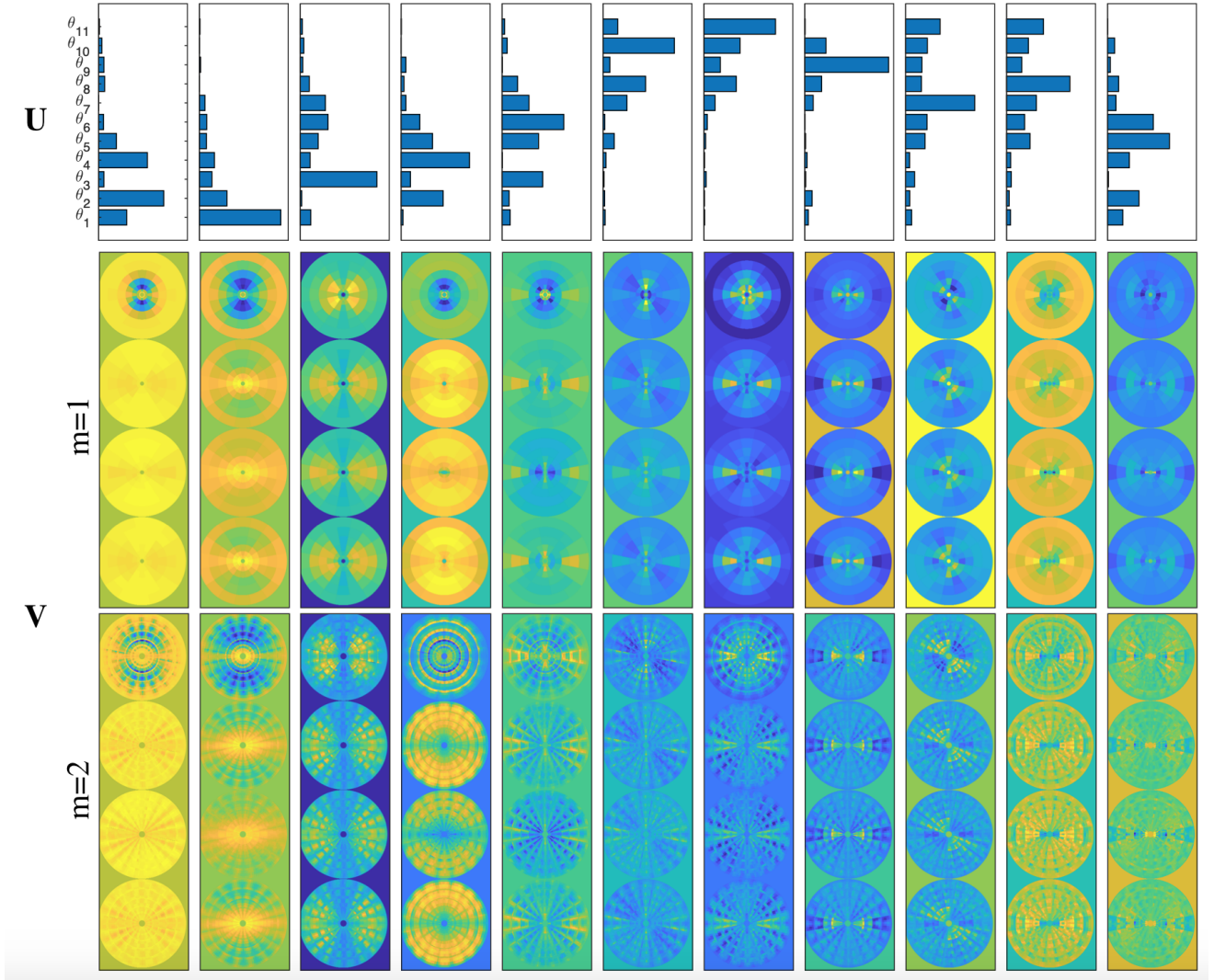


FIG. 10. Orthogonal basis vectors, \mathbf{U} (top panel) and \mathbf{V} (bottom panel), which map the model parameters and scattering coefficients, respectively, into the directly correlated space. For the scattering coefficients, the first order is shown in the top row and the second order in the bottom row.

for model training, the validation set is used for cross-validation and model selection, while the test set is set aside and used to assess the performance of the selected model.

The scatter plots in Fig. 12 and Fig. 13 show predicted vs. actual morphological parameters of the test set in the \log_{10} -scaled MST coefficient space. There is reasonable agreement over a large range of parameter space. The correlation is very diagonal and close to 1, and the regression coefficient is quite good, $R^2 = 0.91$. This all shows that the regression is performing very well.

E. Metric design verification

Table II shows cross validation results which aided in the design of the MST metric. The *base* metric was constructed using the aforementioned design criteria, most of

which were inherited from previous image classification applications of the MST. We found a modest improvement in performance when using a much larger training set (four times bigger). From our cross validation, there was a modest drop in performance when not \log_{10} -scaling the MST coefficients, not using the second order MST ($m = 1$ only), using integrated intensity instead of max value normalization, and decreasing the number of MST filter rotations.

IV. APPLICATIONS AND RESULTS

There are two primary cases of interest for applying our method. The first is to be able to quantitatively compare experimental data to simulation. The second is to be able to compare morphology between different

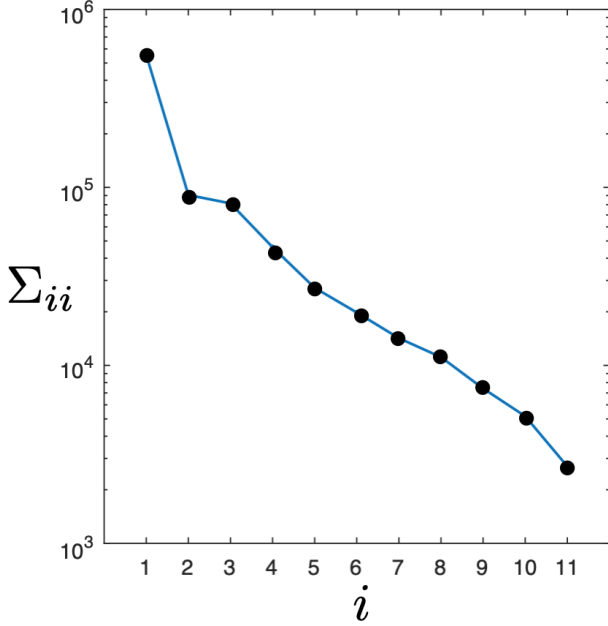


FIG. 11. Singular values of the cross-covariance matrix, given by the diagonal elements of Σ . Gives the significance of the orthogonal vectors of Fig. 10.

TABLE II. Cross-Validation results. All models are slight deviations from the Base Model defined by 2048 training images, max normalization, $m=2$, 4×4 -gridding, 8 rotations and \log_{10} -features.

Model	Validation Set R^2
Base	0.9094
8192 training images	0.9237
$m = 1$	0.7238
4 rotations	0.8449
non- \log_{10} on features	0.8752
integrated intensity normalization	0.8849

experiments and quantify what those differences are. In doing so, we will be able to make statistically sound inferences about discrepancies in morphology. By providing this capability, the method will provide physical insight into the physical mechanisms causing the differences. To this end, we conduct some initial studies which show how the method will be used.

A. Simulation-to-experiment comparison

The experimental images are obtained from the Continuum X-ray Imager instrument fielded on Z.³ We include self emission images from an AR4.5, AR6 and AR9 MagLIF experiments fielded on Sandia’s Z-Machine – experiments z3017, z2839 and z3018, respectively. Here, the Aspect Ratio (AR) is the ratio of the outer liner radius to the liner thickness. For each of the experimental

images, synthetic radiographs are taken from 3D radiation magnetohydrodynamic (rad-MHD) GORGON¹⁹ simulations modeling a corresponding experiment. These simulations are run with continuous virtual boundary edges at a height of 5 mm and the synthetic radiographs are calculated using a ray-tracing algorithm onto a virtual image plate. The experimental images have been vertically cropped down to a 5 mm height to compare with their simulated counterparts. The experimental images continue to have similar structure over their full height of about 1 cm. Figure 14 shows the comparison of simulated and experimental self emission images at several different liner aspect ratios.

There are distortions to both the experimental and simulation x-ray self emission images. For the experimental images there are instrumental responses, noises, and calibrations that can not be explicitly estimated. For the simulations there are approximations to the physics, and numerical error in the calculations. This leads to the “true” image being shifted into different *domains* for the experiments and the simulations. In order to address this discrepancy, we have developed a *background subtraction* method. The method works by projecting out a background vector \mathbf{B}_1 given by the first principal component of the covariance between simulation and experiment, such that $\tilde{S}_{\text{domain}}^{\text{AR}} = S_{\text{domain}}^{\text{AR}} - \text{proj}(S_{\text{domain}}^{\text{AR}}, \mathbf{B}_1)$, where AR is the aspect ratio, and the domain represents whether the features are from simulated or experimental images.

This process of background subtraction is demonstrated in Fig. 15. The MST coefficients for the AR4.5 case are shown for the simulated and experimental data in the left two columns of the figure. There are apparent qualitative similarities of the MST coefficients between the two cases. However, there is some nontrivial background present in the experimental data, which our approach projects out. Specifically, if we take the first principal component of the covariance between simulation and experiment, we find the center column of Fig. 15 – the background, \mathbf{B}_1 . After projecting out this background component from the experimental data (the right two columns of Fig. 15), we can observe similarities and differences between the simulation and experimental morphologies by comparing the overall separation of the scattering coefficients, R_{kl}^2 , computed as pairwise Euclidean distances, σ_{kl} , normalized by the average intra AR class distance,

$$R_{kl}^2 = \frac{\sigma_{kl}^2}{\text{mean}(\sigma_{ii}^2)}. \quad (24)$$

where k and l refer to the AR index of simulation and experiment, respectively. We can then visualize how well separated they are by plotting

$$\Omega_{kl} = N_l e^{-|R_{kl}|}, \quad (25)$$

which is analogous to the surrogate confusion matrix, Ω_{ij} , defined in Eq. (13). Precision and separation can be

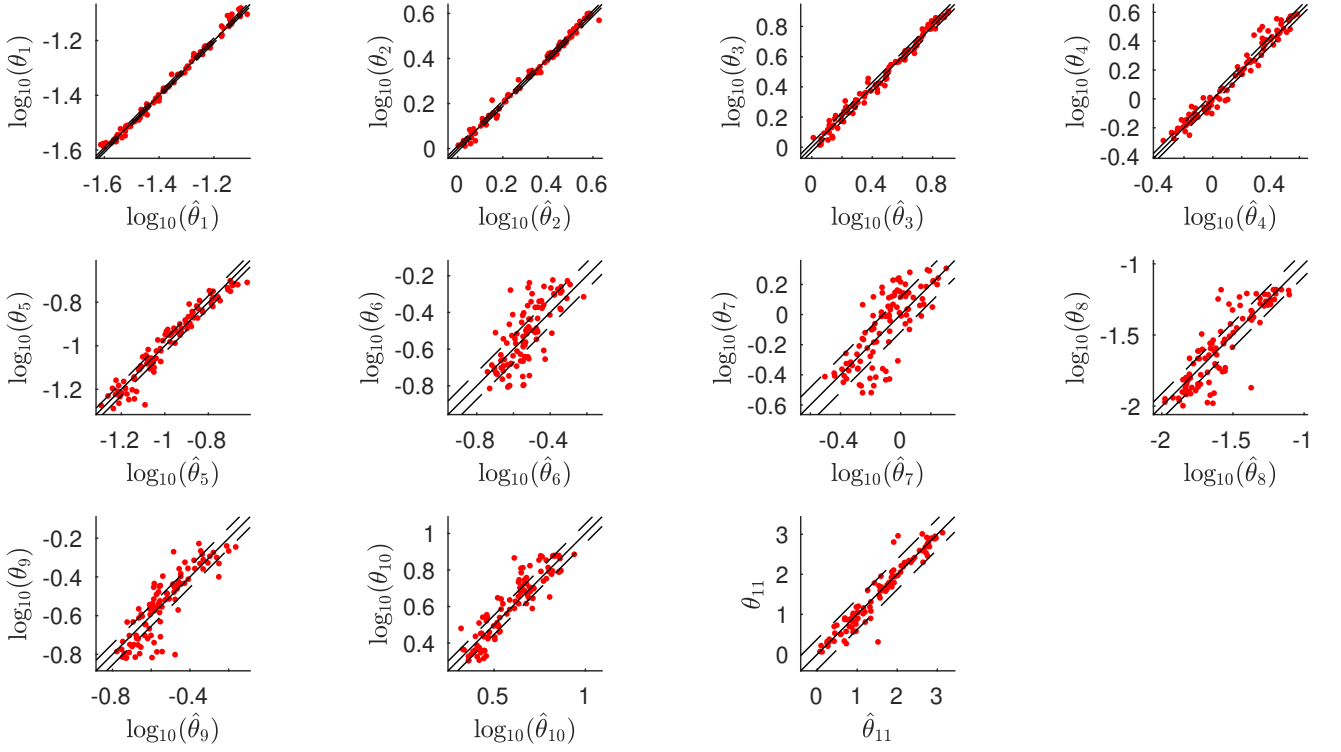


FIG. 12. MST regressor performance. The scatter plots show predicted vs. actual parameters in \log_{10} -space. The first several demonstrate very good performance, while the later components show slightly less performance. This may be indicative of nonlinearity which the linear regression cannot explain, or it may be variance caused by the unexplained ζ parameters.

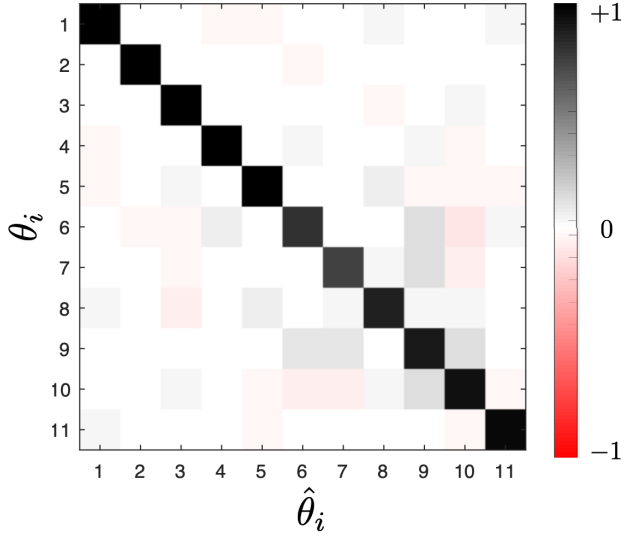


FIG. 13. Further look at the MST regressor performance. Correlation plot which shows that the correlation of the predicted parameters to the actual parameters is very diagonal and close to 1.

similarly be defined. The effectiveness of the background subtraction is quantified by an improvement in the precision from 0.40 to 0.08, and an increase in the separation

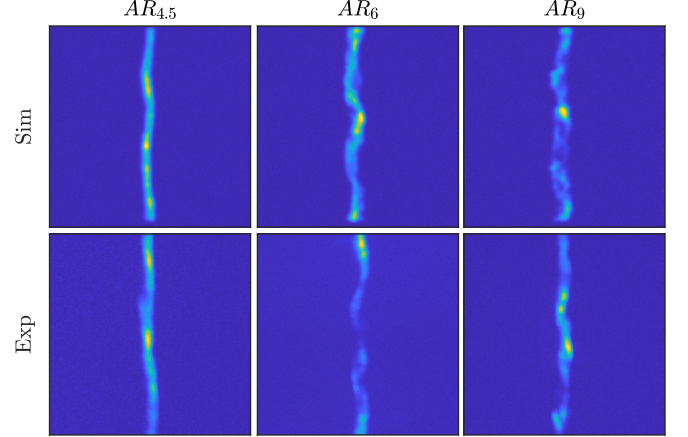


FIG. 14. Stagnation images from selected MagLIF experiments at varying aspect ratios and their corresponding simulated counterparts.

from 1.9 to 4.8.

The quantification of the similarities and differences between the simulations and experiments is shown in Fig. 16. This demonstrates that the simulations are generally close in MST space to the corresponding experiment, with AR4.5 simulation showing some pairwise similarity to the AR9 experiment.

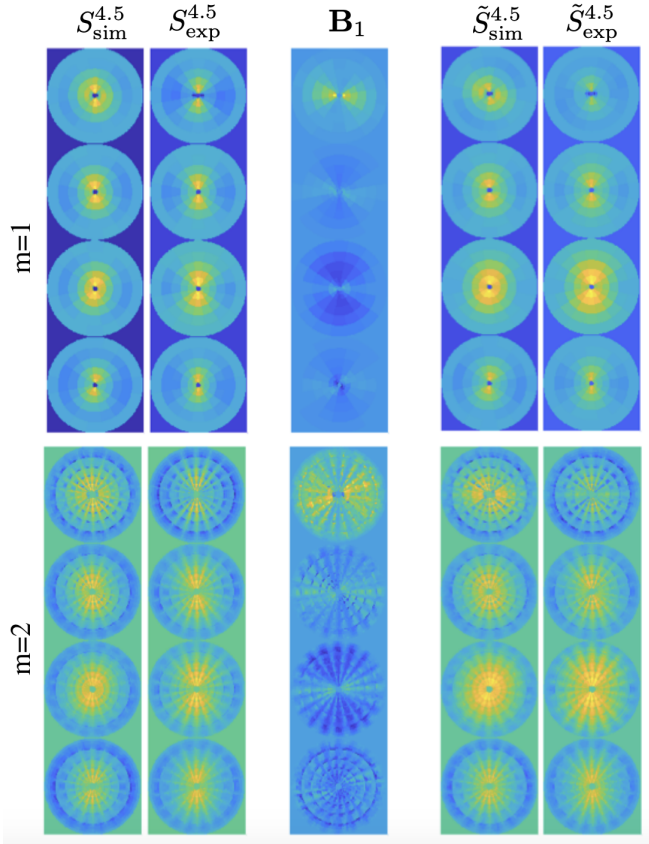


FIG. 15. Background Subtraction. The top row are the first order MST coefficients, and the second row are the second order MST coefficients. The two columns on the left are before the background is projected out, the center column is the background derived from the first principal component of the covariance between simulation and experiment, and the right two columns are after the background is projected out. This is for the AR4.5 case.

B. Experiment-to-experiment comparison and analysis

Finally, we finish with a discussion of differentiating morphology between experiments. Figure 17 shows the experimental plasma stagnation columns along side the synthetic model for the mean prediction and their first and second order MST coefficients of two different liner designs. To the left is experiment z3236 which utilized a dielectric coated AR9 target, while to the right is experiment z3289 which had an uncoated AR6 liner. The dielectric coating on the exterior of the liner is expected to reduce the amount of magnetic Rayleigh-Taylor growth by reducing the electro-thermal instability that is seeding it. There are other significant differences between these two experiments in the amplitude of the current drive, preheating laser pulse profile, applied axial magnetic field, magnetic field axial uniformity, and liner configurations. There are obvious differences between the MST coefficients for the two cases; but what is different? To answer this question, we applied the regression

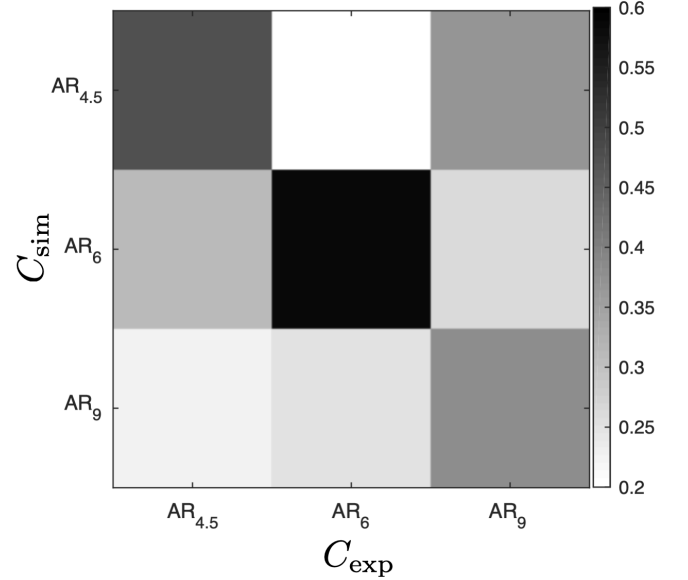


FIG. 16. The surrogate confusion matrix Ω_{kl} defined by Eq. (25) quantifying similarities and differences between the simulations (“sim”) and experiments (“exp”). Probability of classifying as C_{sim} given that it is C_{exp} , $P(C_{\text{sim}}|C_{\text{exp}})$, is plotted as the image.

derived in Sec. III D. The regressed synthetic parameters and their uncertainties for MagLIF experiments z3236 and z3289 are shown in Table III. The listed uncertainties represent the 95% confidence intervals and are obtained from the multivariate Gaussian distribution of the test data, $\{\mathbf{Y}_{\text{pred},i}\}_{i=1}^{N_{\text{resamp}}}$. The estimates of selected parameters of the synthetic helical model, the θ 's, along with their uncertainties, are plotted for the two cases side-by-side in Fig. 18. For parameters such as helical radius and the amplitude of the high frequency axial brightness perturbations, there are negligible differences. For other parameters such as the strand thickness, there are modest differences. For yet other parameters such as strand length, helical wavelength, amplitude of the low frequency axial brightness perturbations, the wavelength of the low frequency axial brightness perturbations, and the wavelength of the high frequency axial brightness perturbations; there are significant differences. The reader will also note that the synthetic images given by the mean prediction capture a number of physical features such as the helical wavelength reasonably well.

V. CONCLUSIONS

We have designed and optimized a metric of stagnation morphology using the MST. This was based on both classification of ensembles of synthetic stagnation images, and regression of those synthetic stagnation images to the morphology parameters used to generate them. Excellent performance of both the classifier and regressor

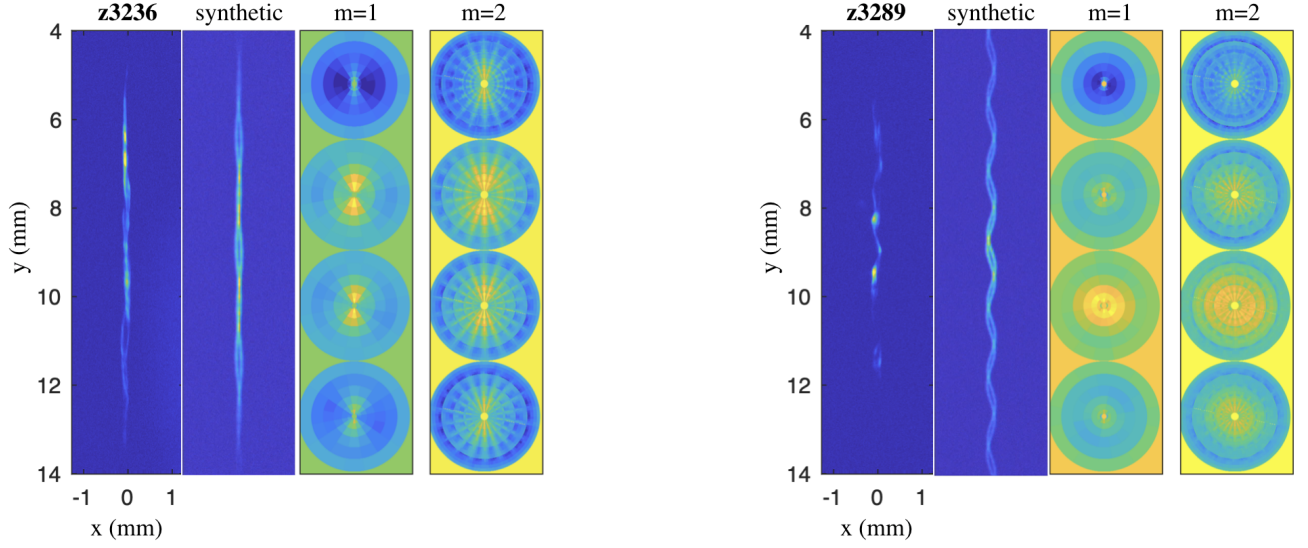


FIG. 17. Comparison of two experiments using the MST. To the left is shot z3236 with a coated AR9 liner. To the right is shot z3289 with an uncoated AR6 liner. Shown, for both cases, are the original stagnation image on the left, the MAP synthetic image, and the MST on the right (both first and second order coefficients). Ensemble of fit synthetics (Multimedia View, for z3236) and (Multimedia View, for z3289). Shown are the experimental image (left), and member of ensemble of fit synthetics (right).

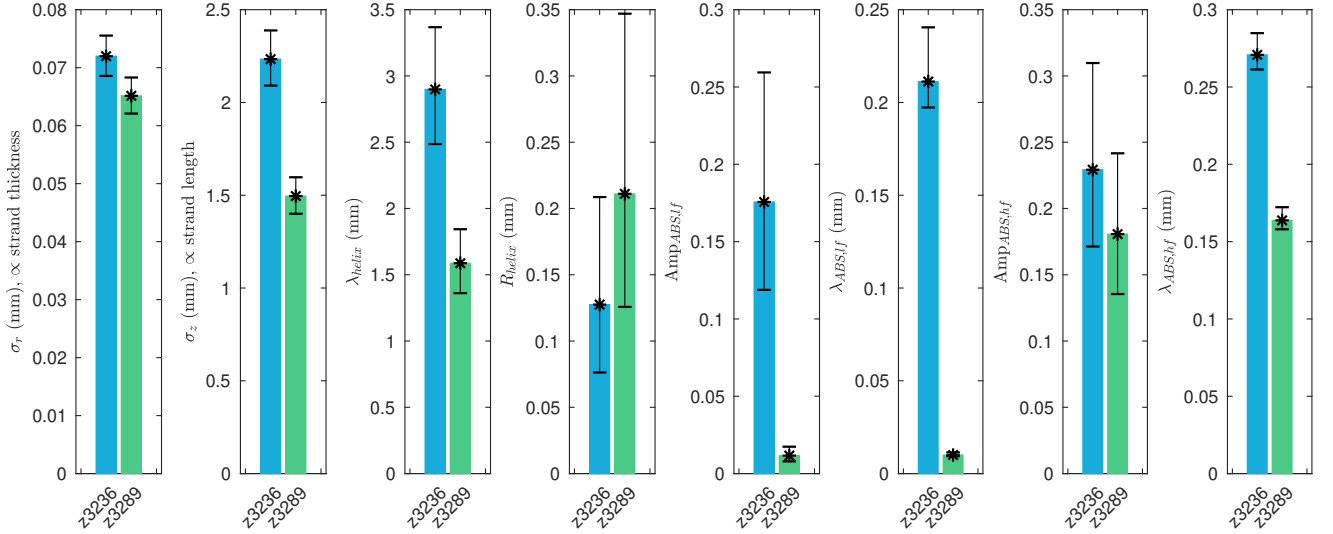


FIG. 18. Regressed parameters of the synthetic helical model for the two experiments shown in Fig. 17. The values for shot z3236 are shown in blue on the left, and for shot z3289 in green on the right. Plotted are modes with error bars showing the 95% confidence interval. The error bars are asymmetric because this is not in log space. The parameters are (from left to right): strand thickness (mm), strand length (mm), helical wavelength (mm), radius of the helix (mm), amplitude of the low frequency axial brightness perturbations, wavelength of the low frequency axial brightness perturbations, amplitude of the high frequency axial brightness perturbations, and wavelength of the high frequency axial brightness perturbations.

was obtained. We demonstrated that the MST provides a convenient basis in which to project out discrepancies between simulated and experimental images. This metric is then able to be used to test hypotheses, such as if the AR of the liner makes significant changes to the stagnation morphology, and whether the rad-MHD computer simulations predict the changes to the stagnation mor-

phology. Finally, the regression enabled the morphology parameters of the stagnation to be estimated with uncertainty. It should be noted that nonlinear aspects of this regression were captured by including more components of the MST SVD vectors in the linear regression of the MST to the morphological parameters.

The MST metric space does look to be a low dimen-

TABLE III. MST Regressor determined stagnation column morphological parameters from MagLIF experiments z3236 and z3289.

	z3236	z3289
	Coated AR9	Uncoated AR6
θ_1	$0.0720 + (-0.0034, 0.0036)$	$0.0651 + (-0.0031, 0.0032)$
θ_2	$2.2335 + (-0.1425, 0.1546)$	$1.4954 + (-0.0950, 0.1013)$
θ_3	$2.1677 + (-0.3083, 0.3509)$	$3.9584 + (-0.5638, 0.6389)$
θ_4	$1.5327 + (-0.2560, 0.3003)$	$0.3120 + (-0.0509, 0.0622)$
θ_5	$0.0988 + (-0.0145, 0.0176)$	$0.1975 + (-0.0282, 0.0337)$
θ_6	$0.1756 + (-0.0568, 0.0838)$	$0.0116 + (-0.0037, 0.0058)$
θ_7	$6.8597 + (-3.1944, 5.8555)$	$79.247 + (-36.568, 68.318)$
θ_8	$0.0286 + (-0.0107, 0.0175)$	$0.0136 + (-0.0051, 0.0084)$
θ_9	$0.2293 + (-0.0579, 0.0805)$	$0.1807 + (-0.0452, 0.0609)$
θ_{10}	$5.3522 + (-1.3159, 1.7144)$	$4.8469 + (-1.1991, 1.5604)$
θ_{11}	$0.4819 + (-0.4050, 0.4027)$	$2.0195 + (-0.4009, 0.4079)$

sional representation of the stagnation images. The affine classifier showed little improvement after about 4 dimensions, and the SVD of the cross variance of the morphology parameters of the synthetic model and the MST contained most of the variance within the first four components.

There are several ways that this research can be improved and expanded upon. The model has been trained on an inherently 2D synthetic data set whereas the experimental images are projections of complex 3D physical systems onto 2D image plates. The synthetic model also has a significant amount of symmetry that is not seen in the experimental images. This work could be expanded to use a 3D synthetic model with less symmetry, to address these issues. Although the use of more components of the MST SVD vectors did reduce the nonlinear artifacts of the linear regression, one could apply some of the modern nonlinear regressions, both shallow and deep. There are still some experimental images which are too noisy, or exhibit other artifacts which preclude our ability to get reliable morphology parameter estimates. Additional machine learning and data augmentation methods as well as using a larger data base of experimental images could address this issue.

The connection of the MST to the underlying physics of the rad-MHD, and its emergent behavior is being explored by our ongoing research.^{16,17} For example, we are addressing questions such as: what is the formal connection of the MST to physical dynamics of both classical and quantum field systems? Can a surrogate for the rad-MHD evolution be constructed using the MST, and can the fixed point, that is, emergent behavior be extracted from that surrogate? What is the expression of helicity and energy in the MST space? What is the relationship of the MST to algebraic topology, that is concepts such as manifold curvature and the Atiyah-Singer index theorem?²⁰

Finally, we emphasize that the *background subtraction* in the MST metric space is essential to obtain a quantitative metric which can be used to compare morphology

of simulation and experiment. By studying the variation between and within datasets in this metric space, the distortions and system responses can be characterized and removed. The simple case that we presented in Sec. IV A, using only six samples, demonstrated its potential, but extensions of this work to much larger datasets in future work will provide further clarification on the usefulness of the background subtraction procedure.

VI. ACKNOWLEDGMENTS

We would like to thank Stéphane Mallat for many useful discussions, suggestions, and providing a computer software implementation of his Scattering Transformation. This research was funded by the Sandia National Laboratories' Laboratory Directed Research and Development (LDRD) program. Sandia National Laboratories is a multimission laboratory managed and operated by National Technology and Engineering Solutions of Sandia LLC (NTESS), a wholly owned subsidiary of Honeywell International Inc., for the U.S. Department of Energy's National Nuclear Security Administration (NNSA) under contract DE-NA0003525. This paper describes objective technical results and analysis. Any subjective views or opinions that might be expressed in the paper do not necessarily represent the views of the U.S. Department of Energy or the United States Government.

- ¹S. A. Slutz, M. C. Herrmann, R. A. Vesey, A. B. Sefkow, D. B. Sinars, D. C. Rovang, K. J. Peterson, and M. E. Cuneo, *Physics of Plasmas* **17** (2010), 10.1063/1.3333505.
- ²T. J. Awe, R. D. McBride, C. A. Jennings, D. C. Lamppa, M. R. Martin, D. C. Rovang, S. A. Slutz, M. E. Cuneo, A. C. Owen, D. B. Sinars, K. Tomlinson, M. R. Gomez, S. B. Hansen, M. C. Herrmann, J. L. McKenney, C. Nakhleh, G. K. Robertson, G. A. Rochau, M. E. Savage, D. G. Schroen, and W. A. Stygar, *Physical Review Letters* **111**, 1 (2013).
- ³M. R. Gomez, S. A. Slutz, A. B. Sefkow, D. B. Sinars, K. D. Hahn, S. B. Hansen, E. C. Harding, P. F. Knapp, P. F. Schmit, C. A. Jennings, T. J. Awe, M. Geissel, D. C. Rovang, G. A. Chandler, G. W. Cooper, M. E. Cuneo, A. J. Harvey-Thompson, M. C. Herrmann, M. H. Hess, O. Johns, D. C. Lamppa, M. R. Martin, R. D. McBride, K. J. Peterson, J. L. Porter, G. K. Robertson, G. A. Rochau, C. L. Ruiz, M. E. Savage, I. C. Smith, W. A. Stygar, and R. A. Vesey, *Physical Review Letters* **113**, 1 (2014).
- ⁴R. D. McBride, S. A. Slutz, C. A. Jennings, D. B. Sinars, M. E. Cuneo, M. C. Herrmann, R. W. Lemke, M. R. Martin, R. A. Vesey, K. J. Peterson, A. B. Sefkow, C. Nakhleh, B. E. Blue, K. Killebrew, D. Schroen, T. J. Rogers, A. Laspe, M. R. Lopez, I. C. Smith, B. W. Atherton, M. Savage, W. A. Stygar, and J. L. Porter, *Phys. Rev. Lett.* **109**, 135004 (2012).
- ⁵C. E. Seyler, M. R. Martin, and N. D. Hamlin, *Physics of Plasmas* **25**, 062711 (2018), <https://doi.org/10.1063/1.5028365>.
- ⁶D. J. Ampleford, C. A. Jennings, E. C. Harding, M. R. Gomez, T. Webb, P. Schmit, T. J. Awe, P. F. Knapp, A. J. Harvey-Thompson, M. R. Weis, S. A. Slutz, S. B. Hansen, G. A. Chandler, G. Dunham, M. Geissel, J. Fisher, D. F. adn M. E. Glin-sky, K. D. Hahn, D. Lamppa, L. Lucero, M. Mangan, M. Martin, T. Moore, R. Paguio, L. Perea, G. Robertson, C. Ruiz, G. E. Smith, I. C. Smith, C. S. Speas, K. Whittemore, E. Yu, R. McBride, B. Jones, K. J. Peterson, G. A. Rochau, and D. B. Sinars, "Improved morphology and reproducibility of Magnetized Liner Inertial Fusion experiments," (2019), in preparation for *Physics of Plasmas*.

- ⁷J. Taylor, *Reviews of Modern Physics* **58**, 741 (1986).
- ⁸D. Yager-Elorriaga, P. Zhang, A. Steiner, N. Jordan, Y. Lau, and R. Gilgenbach, *Physics of Plasmas* **23**, 101205 (2016).
- ⁹S. Mallat, *Communications on Pure and Applied Mathematics* **65**, 1331 (2012).
- ¹⁰J. Bruna and S. Mallat, *IEEE Transactions on Pattern Analysis and Machine Intelligence* **35**, 1872 (2013), arXiv:1203.1513.
- ¹¹Y. le Cun, “Generalization and network design strategies. Technical Report CRG-TR-89-4,” Tech. Rep. (University of Toronto, Department of Computer Science, 1989).
- ¹²F. Ning, D. Delhomme, Y. le Cun, F. Piano, L. Bottou, and P. Barbano, *IEEE Transactions on Image Processing* **14**, 1360 (2005).
- ¹³I. Goodfellow, J. Pouget-Abadie, M. Mirza, B. Xu, D. Warde-Farley, S. Ozair, A. Courville, and Y. Bengio, in *Advances in neural information processing systems* (2014) pp. 2672–2680.
- ¹⁴Y. LeCun, K. Kavukcuoglu, and C. Farabet, in *International Symposium on Circuits and Systems (ISCAS 2010), May 30 - June 2, 2010, Paris, France* (2010) pp. 253–256.
- ¹⁵J. A. Krommes, *Physics Reports* **360**, 1 (2002).
- ¹⁶M. E. Glinsky, T. W. Moore, W. E. Lewis, M. R. Weis, C. A. Jennings, D. A. Ampleford, E. C. Harding, P. F. Knapp, M. R. Gomez, and S. E. Lussiez, “Quantification of maglif morphology using the mallat scattering transformation,” Tech. Rep. SAND2019-11910 (Sandia National Laboratories, 2019) arXiv:1911.02359.
- ¹⁷M. E. Glinsky, “A new perspective on renormalization: the scattering transformation,” (2011), arXiv:1106.4369.
- ¹⁸C. M. Bishop, *Pattern recognition and machine learning* (Springer, 2006).
- ¹⁹J. P. Chittenden, S. V. Lebedev, C. A. Jennings, S. N. Bland, and A. Ciardi, *Plasma Physics and Controlled Fusion* **46** (2004), 10.1088/0741-3335/46/12B/039.
- ²⁰M. F. Atiyah and I. M. Singer, *Bulletin of the American Mathematical Society* **69**, 422 (1963).